

# Facile Design of Oxide-Derived Cu Nanosheet Electrocatalyst for CO<sub>2</sub> Reduction Reaction

Juhee Jang<sup>1</sup>, Shangqian Zhu<sup>1</sup>, Ernest Delmo<sup>1</sup>, Tiehuai Li<sup>1</sup>, Qinglan Zhao<sup>1</sup>, Yinuo Wang<sup>1</sup>, Lili Zhang<sup>2</sup>, Jingjie Ge<sup>1</sup>, and Minhua Shao<sup>1</sup>

<sup>1</sup>Hong Kong University of Science and Technology School of Engineering

<sup>2</sup>Huaiyin Normal University Jiangsu Key Laboratory for Chemistry of Low-Dimensional Materials

December 21, 2022

## Abstract

Despite of superior performance of the oxide-derived copper (OD-Cu) in producing valuable hydrocarbons during CO<sub>2</sub>RR, its fabrication process is still ambiguous and complicated. In this work, we develop a simple microwave-assisted method to synthesize the oxide-derived Cu nanosheet (OD-Cu NS) and reveal that the oxidation state of Cu species is controlled by varying the Cu precursor amount. Notably, the simultaneous formation of nano-sized Cu domains influence the surface roughness of OD-Cu NS. The partially oxidized Cu surface exhibits a superior faradaic efficiency (FE) of C<sub>2+</sub> products up to 72%, along with a partial current density of 55 mA cm<sup>-2</sup> in a neutral KHCO<sub>3</sub> solution. More importantly, the as-obtained OD-Cu NS shows a synergetic effect on dissociating of CO<sub>2</sub> molecules by the strong binding energy and promoting of C<sub>2+</sub> compounds productivity by the enlarged electrochemical surface area. This work provides a new insight for designing efficient OD-Cu catalysts towards CO<sub>2</sub>RR.

## Facile Design of Oxide-Derived Cu Nanosheet Electrocatalyst for CO<sub>2</sub> Reduction Reaction

Juhee Jang<sup>1</sup>, Shangqian Zhu<sup>1</sup>, Ernest Pahuyo Delmo<sup>1</sup>, Tiehuai Li<sup>1</sup>, Qinglan Zhao<sup>1</sup>, Yinuo Wang<sup>1</sup>, Lili Zhang<sup>2</sup>, Jingjie Ge<sup>1,3,5,\*</sup> and Minhua Shao<sup>1,3,4,\*</sup>

<sup>1</sup>Department of Chemical and Biological Engineering, The Hong Kong University of Science and Technology, Clear Water Bay, Kowloon, Hong Kong, China

<sup>2</sup>Jiangsu Key Laboratory for Chemistry of Low-Dimension Materials, Huaiyin Normal University, Huaian 223300, Jiangsu, China

<sup>3</sup>Energy Institute, The Hong Kong University of Science and Technology, Clear Water Bay, Kowloon, Hong Kong, China

<sup>4</sup>Chinese National Engineering Research Center for Control & Treatment of Heavy Metal Pollution, The Hong Kong University of Science and Technology, Clear Water Bay, Kowloon, Hong Kong, China

<sup>5</sup>HKUST Jockey Club Institute for Advanced Study, The Hong Kong University of Science and Technology, Clear Water Bay, Kowloon, Hong Kong, China

\*Corresponding authors

jjge@ust.hk; kemshao@ust.hk

## ABSTRACT

Despite of superior performance of the oxide-derived copper (OD-Cu) in producing valuable hydrocarbons during CO<sub>2</sub>RR, its fabrication process is still ambiguous and complicated. In this work, we develop a simple microwave-assisted method to synthesize the oxide-derived Cu nanosheet (OD-Cu NS) and reveal that the oxidation state of Cu species is controlled by varying the Cu precursor amount. Notably, the simultaneous formation of nano-sized Cu domains influence the surface roughness of OD-Cu NS. The partially oxidized Cu surface exhibits a superior faradaic efficiency (FE) of C<sub>2+</sub> products up to 72%, along with a partial current density of 55 mA cm<sup>-2</sup> in a neutral KHCO<sub>3</sub> solution. More importantly, the as-obtained OD-Cu NS shows a synergetic effect on dissociating of CO<sub>2</sub> molecules by the strong binding energy and promoting of C<sub>2+</sub> compounds productivity by the enlarged electrochemical surface area. This work provides a new insight for designing efficient OD-Cu catalysts towards CO<sub>2</sub>RR.

## Introduction

Fast industrialization and economic growth have aroused huge consumption of fossil fuels and released a large amount of carbon dioxide (CO<sub>2</sub>) into the atmosphere,<sup>1,2</sup> which has caused global warming issues and serious climate change. The electrochemical CO<sub>2</sub>reduction reaction (CO<sub>2</sub>RR), which converts CO<sub>2</sub> to various value-added chemicals, has drawn wide interest as a promising approach for the management of CO<sub>2</sub> emission. Particularly, C<sub>2+</sub> molecules are regarded as highly valuable products due to their applications in wide industrial field.<sup>3-6</sup> Since Hori et al. firstly reported that Cu foil has unique properties to generate various hydrocarbons products beyond 2e<sup>-</sup> reduction pathway,<sup>7,8</sup> Cu-based catalysts have been explored extensively. The constraints in the bulk Cu foils,<sup>9</sup> such as low selectivity, high overpotentials, insufficient stability, and strong competition from the hydrogen evolution reaction (HER), were addressed by Cu-based nanocatalysts with modified structures,<sup>10,11</sup> tuned crystal facets,<sup>12</sup> regulated the compositions with other metal elements and/or organic molecules, etc.<sup>13-15</sup>

Among various types of Cu-based nanocatalysts, the oxide-derived copper (OD-Cu) has shown great potential for producing the value-added multi-carbon compounds.<sup>16</sup> Notably, the chemical state of Cu<sup>+</sup>, i.e., the partially oxidized Cu on the surface of OD-Cu, could modify the electronic structure of active sites, thereby lead to a strong binding energy with one of the most crucial intermediates \*CO, and further promote those dimerization to produce multicarbon compounds.<sup>17,18</sup> Therefore, various methods have been developed to fabricate the partially oxidized Cu<sup>+</sup> state for enhancing the productivity of C<sub>2+</sub> hydrocarbons. For instance, a thin CuO<sub>x</sub> sheath on the surface of OD-Cu nanowires was formed by slowly oxidized in air atmosphere and reached up to 78% of FE for C<sub>2+</sub> products.<sup>19</sup> In addition, by using the O<sub>2</sub> plasma treated Cu nanocubes, the selectivity of C<sub>2</sub>H<sub>4</sub> and the current density in CO<sub>2</sub>RR were enhanced compared to that under Ar plasma treatment.<sup>20</sup> Besides the oxidation state, the role of surface roughening on the OD-Cu was also examined to enrich the catalytic active sites.<sup>21-25</sup> The roughened surface possesses abundant interfaces, grain boundaries, and low coordinated sites, which are generally regarded as the active sites to trap the key intermediate \*CO and initiate the dimerization step.<sup>19</sup> However, the existing post-treatments on the pristine Cu such as plasma irradiation,<sup>10</sup> air-oxidation,<sup>26</sup> and electropolishing<sup>27</sup> are still difficult to well-controllably synthesize OD-Cu. A facile method to efficiently fabricate the OD-Cu nanocatalysts is highly desired.<sup>18,28</sup>

Herein, we explored a simple microwave heating procedure to synthesize OD-Cu nanosheets (OD-Cu NSs) and revealed how adding extra Cu precursor affected the development of the surface Cu<sup>+</sup> state by increasing the surface roughness. Impressively, the optimized OD-Cu NS with 30 wt% of extra-added Cu precursor, denoting as Cu-30, achieved the faradaic efficiency (FE) of 72% and the geometric current density of 31 mA cm<sup>-2</sup> for C<sub>2+</sub> products at -1.1 V<sub>RHE</sub>. Furthermore, the electrochemical surface area (ECSA) of the as-obtained Cu-30 with a rough surface is about five times over the pristine CuO NS. This works provides insights about the relationship between the binding energy of \*CO intermediate on the surface of Cu-30 with the specific chemical state of the partially oxidized Cu by the means of inspection of OH<sup>-</sup>adsorption.

## Experiments

*Chemicals and Materials* . All chemicals were used without further purification. Deionized water (DI water) with a resistivity of 18.2 MΩ·cm (Millipore) was used. Copper chloride dihydrate (CuCl<sub>2</sub>·2H<sub>2</sub>O, 99.0%),

aqueous hydrogen peroxide ( $\text{H}_2\text{O}_2$ , 30% w/w in  $\text{H}_2\text{O}$ ), potassium hydrogen carbonate ( $\text{KHCO}_3$ , 99.7%), 5% Nafion solution, isopropanol, ethanol, ethylene glycol (anhydrous, 99%), dimethyl sulfoxide (anhydrous, 99.5%), and phenol (99%) were supplied by Sigma Aldrich. Copper nitrate trihydrate ( $\text{CuNO}_3 \cdot 3\text{H}_2\text{O}$ , 99.99%) and sodium hydroxide ( $\text{NaOH}$ , 99.99%) were purchased from Aladdin and VWR Chemicals, respectively.  $\text{D}_2\text{O}$  (99.9% atom%D) was purchased from J&K Chemicals.

*Synthesis of OD-Cu NS*. The pristine CuO nanosheets (NSs) were synthesized by following a procedure previously reported by Zhang et al.<sup>29</sup> 85.2 mg of  $\text{CuCl}_2 \cdot 2\text{H}_2\text{O}$  was dispersed into 10 ml of 3 M NaOH solution by vigorous stirring, then transferred into the Teflon-liner stainless steel autoclave. After kept at 100 °C for 12 hours in the oven and then cooled down to room temperature, the obtained product was washed by DI water and ethanol for four times respectively and dried at 80 °C under the vacuum oven for overnight. To prepare the OD-Cu NS, 20 mg of the as-synthesized CuO NS with 30 wt% (Cu-30) or 100 wt% (Cu-100)  $\text{Cu}(\text{NO}_3)_2 \cdot 3\text{H}_2\text{O}$  was suspended into 10 ml of ethylene glycol, then transferred into a Pyrex glass bottle. The mixture solution was ultrasonicated in ice water for 1 hour, then moved into the digestive microwave (Milestone, Ethos One) with the power of 1050 W for 210 s under an ambient atmosphere. The dark brownish colored precipitate was cooled to room temperature and then collected by centrifugation. Subsequently, the dark brownish precipitate was collected by a centrifuge process at 15000 rpm for 10 mins, and washed four times by ethanol. After dried under a vacuum oven at 60 °C overnight, the obtained OD-Cu NS were collected for further usage.

*Physical Characterizations*. Transmission electron microscopy (TEM) images were recorded on a JEOL JEM-2010F (JEOL, Tokyo, Japan). Aberration-corrected TEM was operated on JEOL JEM-ARM200F at 200kV acceleration voltage. The samples used for TEM characterization were dispersed in absolute ethanol firstly, then dropped onto carbon coated Cu or Ni grid and dried completely at room temperature. The X-ray diffraction (XRD) patterns were recorded at room temperature with an X'pert Pro K-Alpha diffractometer (PANalytical, Almelo, Netherlands), using Cu  $K\alpha$  radiation ( $\lambda=1.5406 \text{ \AA}$ ). The XRD samples were prepared by dropping the as-prepared nanoparticles (NPs) suspensions onto a glass slide. The X-ray photoelectron spectroscopy (XPS) was measured by a Physical Electronics 5600 with an Al  $K\alpha$  source ( $h\nu = 1486.6 \text{ eV}$ ), and the fresh samples were used for the XPS measurements to avoid over-oxidation issue.

*Electrochemical Measurement*. To prepare the working electrode, 2 mg of each catalyst (commercial Cu NP, pristine CuO NS, and OD-Cu NSs) was suspended into 100  $\mu\text{L}$  of absolute ethanol with 5  $\mu\text{L}$  of 5% Nafion solution (Anhydrous, Sigma Aldrich) by ultrasonication. After that, 5  $\mu\text{L}$  of the dispersion was loaded onto a cleaned glassy carbon electrode with a diameter of 5 mm, and dried in ambient atmosphere. For the electrochemical  $\text{CO}_2$ RR measurement, a two-component H-type cell was assembled with a proton exchange Nafion 117 membrane (Aldrich) in the middle. Then each component was filled with 50 ml of 0.1 M  $\text{KHCO}_3$  electrolyte, afterwards  $\text{CO}_2$  gas (99.999%, Asia Pacific Gas Enterprise Co., LTD) was purged into the solution for 1 hour in advance. Platinum (Pt) mesh ( $20 \times 20 \text{ mm}^2$ ) and an Ag/AgCl (saturated into 3.0 M KCl, BASi) electrode were used as a counter and a reference electrode, respectively. The reference electrode was calibrated with 0.1 M  $\text{HClO}_4$  solution (pH 1.1) by reversible hydrogen electrode (RHE) and the potential E was converted to the RHE reference scale in terms of the equation:

$$E \text{ (versus RHE)} = E \text{ (versus Ag/AgCl)} + 0.197 \text{ V} + 0.059 \text{ V} \times \text{pH}.$$

As connecting the gas-tight H-cell to the potentiostat (CHI 627E, CH Instruments, Inc.), iR compensation was conducted automatically at a level of 85%, whereas the rest of 15 % IR drop was manually compensated during data processing.  $\text{CO}_2$  was continuously fed into both parts of the electrolyte via mass flow controllers (Sevenstar, Beijing) at a rate of 30 SCCM. Since trapping air bubbles on the working electrode could cause high resistance, the component containing the working electrode was stirred magnetically at 1500 rpm. The gas products were analyzed by a gas chromatograph (GC2060, Ramiin, Shanghai) equipped with a thermal conductivity detector (TCD) for hydrogen ( $\text{H}_2$ ) quantification and a flame ionization detector (FID) for carbon monoxide (CO), methane ( $\text{CH}_4$ ), and ethylene ( $\text{C}_2\text{H}_4$ ). The calibration curve was obtained by a series of standard gas mixtures ( $\text{H}_2$ , CO,  $\text{CH}_4$ , and  $\text{C}_2\text{H}_4$  balanced in Ar, Shanghai Haizhou Special Gas Co., LTD). Finally, four gas samples at 15, 28, 41, and 54 min were collected and quantified in average for 1

hour electrolysis. Liquid products were collected after the measurement and analyzed by using a Varian 500 MHz  $^1\text{H}$  nuclear magnetic resonance (NMR) spectra. The NMR samples were prepared by mixing 450  $\mu\text{L}$  of electrolyte with 50  $\mu\text{L}$  home-made internal standard solution containing  $500 \times 10^{-6}$  M phenol, and  $100 \times 10^{-6}$  M dimethyl sulfoxide in  $\text{D}_2\text{O}$ . The calibration curves of internal standard solution were established by several standard solutions (0, 50, and 100  $\mu\text{M}$  of formate, methanol, ethanol, acetate, and iso-propanol in 0.1 M  $\text{KHCO}_3$  solution).

The electrochemical activity was examined by linear sweep voltammetry (LSV) from  $-0.1 V_{\text{RHE}}$  to  $-1.8 V_{\text{RHE}}$  in  $\text{CO}_2$  or Ar-saturated 0.1 M  $\text{KHCO}_3$  electrolyte and the electrochemical surface area (ECSA) was measured by cyclic voltammetry (CV) between 0 and  $0.4 V_{\text{RHE}}$  with different scan rates in  $\text{CO}_2$ -saturated 0.1 M  $\text{KHCO}_3$  electrolyte after 1 hour electrolysis by each catalyst. To compare the binding energy of  $\text{OH}^-$  adsorption, LSV curves were obtained from 0.1 to  $0.6 V_{\text{RHE}}$  after the electrolysis in Ar-saturated 0.1 M KOH electrolyte.

## Results and Discussion

The OD-Cu NSs were obtained by a facile microwave irradiation method with a reduction process. In a typical synthesis of Cu-30 and Cu-100, by adding 30 and 100 wt% of  $\text{Cu}(\text{NO}_3)_2 \cdot 3\text{H}_2\text{O}$  to CuO NS, the OD-Cu NSs with a rough surface were formed in a large scale under the microwave irradiation with the power of 1050 W for 210 s. Figure 1a-d show TEM images of the pristine CuO NS (Figure 1a,b), as well as the microwave treated Cu-30 (Figure 1c) and Cu-100 (Figure 1d). The pristine CuO NS has an edge length of hundreds nanometer and smooth surface (Figure 1a,b). After the microwave irradiation, the OD-Cu NSs were obtained exclusively and maintained the original 2D morphology (Figure 1c,d). Interestingly, the nanosized domains (light grey circles in Figure 1c,d) were observed on the surface of Cu-30 and Cu-100 NS. The nuclei of Cu precursor salt could be randomly distributed on the nanosheet due to the polarity of ethylene glycol in a homogeneous mixture, then the copper precursor was rapidly reduced to metallic Cu under the microwave heating and formed the rough surface on the pristine CuO NS.<sup>30</sup>

To figure out their crystal structures, XRD measurements were conducted on the pristine CuO NS, Cu-30, and Cu-100 (Figure 1e). It is clearly shown that the pristine CuO NS consists of pure CuO phase (denoted as #). In comparison, a mixture of metallic Cu and Cu oxide diffraction patterns were observed in Cu-30 and Cu-100. Specifically, the peaks located at  $43.3^\circ$  and  $50.4^\circ$  predominantly in metallic Cu facets (denoted as \*) are corresponding to Cu (111) and (200), respectively. The peaks at  $35.5^\circ$  and  $38.7^\circ$  assigned as CuO (002) and CuO (111) indicated the remains of CuO phase after the microwave process. Because CuO species have a higher dissociative energy than Cu precursors during the microwave-assisted reduction, the XRD patterns of Cu-100 show almost equal peak intensities of metallic Cu and CuO species, indicating that the ratio of oxide phase in Cu-100 was intensified by increasing the amount of  $\text{Cu}(\text{NO}_3)_2 \cdot 3\text{H}_2\text{O}$ .<sup>31,32</sup> Beyond the dissociation energy, the insufficient reductant could further impede the reduction process of CuO NPs since ethylene glycol is rapidly consumed from the preferential reaction with  $\text{NO}_3^-$  and produced  $\text{H}_2\text{O}$  at the initial stage.<sup>32</sup> Additionally, the reductive rate between two distinct Cu species can be affected by the presence of additional Cu salt, resulting in the co-existence of Cu and Cu oxide phases in the OD-Cu NSs.

X-ray photoelectron spectroscopy (XPS) characterization was conducted to identify the surface valence states of Cu (Figure 2) and O (Figure S1). As shown in Figure 2a, all the samples disclosed three distinguished deconvolutions in the spectra of Cu  $2p_{3/2}$ , which can be assigned to  $\text{Cu}^0/\text{Cu}^+$ ,  $\text{Cu}^{2+}$ , and  $\text{Cu}(\text{OH})_2$  species, respectively.<sup>33,34</sup> It was notable that different Cu oxidation states co-existed on the surface of OD-Cu NS samples (Cu-30 and Cu-100). More importantly, the intensity ratio of  $\text{Cu}^0/\text{Cu}^+$  to  $\text{Cu}^{2+}$  for Cu-30 (1.48) is 8 times higher than that for Cu-100 (0.18), demonstrating that Cu-30 surface predominantly consists of  $\text{Cu}^0/\text{Cu}^+$  rather than  $\text{Cu}^{2+}$  species. Furthermore, the Cu  $\text{L}_3\text{M}_{4,5}\text{M}_{4,5}$  Auger region around 568 eV was analyzed to clarify a specific chemical state of Cu element in Figure 2b, since the deconvolution of  $\text{Cu}^0$  or  $\text{Cu}^+$  species is difficult to separate due to their similar binding energies.<sup>29,35</sup> The peak position at 569.7 eV in Cu-30 sample corresponds to  $\text{Cu}^+$  species, whereas the Cu-100 exhibits a positive binding energy shift to  $\text{Cu}^{2+}$  state at 568.8 eV. These Auger XPS results demonstrate the surface of Cu-30 contains a high content of  $\text{Cu}^+$  species despite the absence of  $\text{Cu}_2\text{O}$  signal in the Cu-30 XRD result. Considering previous

reports revealed the relationship between the grain size and detection limitation for XRD inspection, the size of  $\text{Cu}_2\text{O}$  grain was probably too small to be detected.<sup>36</sup> Therefore, the targeted Cu oxidation state was achieved by simply adjusting the Cu salt amount under the microwave irradiation. Due to the surface oxidation from exposure to air, the commercial Cu NPs exhibit a chemical valence of  $\text{Cu}^+$  at 569.6 eV in Cu LMM peak (Figure 2b, black line). Moreover, as shown in Figure S1, the peak of oxygen species in the  $\text{Cu}_2\text{O}$  lattice at 530.5 eV on Cu-30 is distinctly presented in comparison with that of Cu-100 in the O 1s XPS spectra.<sup>37-39</sup>

The electrochemical properties of each catalyst (commercial Cu NPs, CuO NSs, and OD-Cu NSs) were first examined by linear sweep voltammetry (LSV), which are shown in Figure 3a and S2. The LSV curves of these catalysts evidently show higher current densities in the  $\text{CO}_2$ -saturated 0.1M  $\text{KHCO}_3$  than in the Ar-saturated solution, illustrating the benefits from the electrocatalytic activities for  $\text{CO}_2\text{RR}$ . The catalytic  $\text{CO}_2\text{RR}$  performance of the OD-Cu NSs was assessed in the potential window between -0.9 and -1.4  $V_{\text{RHE}}$  in a 0.1 M  $\text{KHCO}_3$  electrolyte. In comparison, the commercial Cu NPs and CuO NSs were also tested. In Figure 3b and S3, the overall FE was presented at each potential and ethylene was detected as the main product for each catalyst. Remarkably, the maximum  $\text{FE}_{\text{C}_2\text{H}_4}$  of 47% was obtained on Cu-30 sample at a low applied potential (both at -1.1 and -1.2  $V_{\text{RHE}}$ ), which is obviously higher than those of Cu NP (26%), CuO NS (40%), and Cu-100 (40%) at the same potential, i.e., -1.1  $V_{\text{RHE}}$  (Figure 4c). Furthermore, as shown in Figure 4c, Cu-30 could reach the highest FE of 72% at -1.1  $V_{\text{RHE}}$  for total  $\text{C}_{2+}$  products ( $\text{C}_2\text{H}_4$ ,  $\text{C}_2\text{H}_5\text{OH}$ ,  $\text{C}_3\text{H}_7\text{OH}$ , and acetate), while only 41%, 58% and 60% were achieved on the commercial Cu NPs, CuO NSs, and Cu-100, respectively. The current density was also improved by Cu-30 during the  $\text{CO}_2\text{RR}$  (Figure 4e and S4). Specifically, the partial current density for  $\text{C}_{2+}$  products ( $j_{\text{C}_{2+}}$ ) of Cu-30 achieved 29  $\text{mA cm}^{-2}$  at -1.1  $V_{\text{RHE}}$ , which is 5 times higher than that of the pristine CuO NSs. The maximum  $j_{\text{C}_{2+}}$  of Cu-30 and Cu-100 reached up to 55 and 52  $\text{mA cm}^{-2}$  at -1.4  $V_{\text{RHE}}$ , respectively, which are higher than 42  $\text{mA cm}^{-2}$  catalyzed by the pristine CuO NSs, illustrating that the metallic Cu phase in OD-Cu produced with the microwave treatment could promote higher conductivity.

Stability is another crucial parameter to evaluate the catalytic performance. The FE on Cu-30 was monitored through continuous electrolysis for 8 hours at -1.1  $V_{\text{RHE}}$ . As shown in Figure S5, the  $\text{FE}_{\text{C}_2\text{H}_4}$  remained > 40% for 8 hours stability test while the sum of FEs for CO and  $\text{CH}_4$  constantly kept less than 10%, suggesting that the production of low-valued products was effectively suppressed on the OD-Cu NSs surface. According to the aforementioned findings, the partially oxidized Cu species on the surface of Cu-30 could promote the \*CO dimerization process, leading to the highest FE for ethylene.

To figure out the catalytic active sites and influential factors toward the improvement of  $\text{FE}_{\text{C}_{2+}}$  on Cu-30 during  $\text{CO}_2\text{RR}$ , the electrochemical surface area (ECSA) was calculated by cyclic voltammetry with different scan speeds under  $\text{CO}_2$ -saturated 0.1 M  $\text{KHCO}_3$  solution after 1 hour catalysis in Figure 4a and S6. By calculating within the double layer charge region, the capacitance values of commercial Cu NPs, CuO NSs, Cu-30, and Cu-100 are 0.48, 1.4, 2.7, and 1.9 mF, respectively. Assuming the theoretical specific capacitance of polycrystalline Cu (pc-Cu) to 29  $\mu\text{F}$ , the surface area of Cu-30 was significantly enhanced to 93  $\text{cm}^2_{\text{ECSA}}$ , much higher than 16.5  $\text{cm}^2_{\text{ECSA}}$  of commercial Cu NPs, 48  $\text{cm}^2_{\text{ECSA}}$  of pristine CuO NSs and 65.5  $\text{cm}^2_{\text{ECSA}}$  of Cu-100.<sup>40</sup> Although the surface morphologies of CuO NSs and Cu-30 are comparable, the ECSA of Cu-30 is twice as large as that of CuO NSs due to the unique partial oxidation state of  $\text{Cu}^+$  surface and the abundant defect sites provided by the nano-domains.<sup>19</sup> Accordingly, the enlarged nano-domains on Cu-30 were obtained after 1 hour electrolysis (Figure S7) and achieved the highest roughness factor of 93 based on defining pc-Cu as one.<sup>41</sup>

It is notable that the dissociation of  $\text{CO}_2$  molecules is one of the rate determining stages, also the energy barrier of  $\text{CO}_2$  decomposition (the absorbed dissociative  $\text{CO}_2$  - \*CO intermediate + the absorbed O) is highly related to the surface oxidative state, especially  $\text{Cu}^+$  and intrinsic defective sites.<sup>42,43</sup> In parallel, the crucial step for the formation of multicarbon products, C-C coupling, is associated with strong binding energy of \*CO intermediates on Cu surface. Considering the dissociative  $\text{CO}_2$  is thermodynamically unstable in the electrolyte, the analysis of  $\text{OH}^-$  adsorption is a surrogate to inspect the binding energy of dissociative

CO<sub>2</sub> adsorption on Cu surface.<sup>42-46</sup> A further investigation for OH<sup>-</sup> adsorption was characterized by the electrochemical measurement in an Ar-saturated 0.1 M KOH electrolyte in the potential window of 0.3-0.6 V<sub>RHE</sub>. As shown in Figure 4b, except for the commercial Cu NPs, the Cu(100) peak (0.2-0.3 V<sub>RHE</sub>) and the Cu(111) shoulder peak around 0.48 V<sub>RHE</sub> were observed on the samples of CuO NSs, Cu-30, and Cu-100.<sup>43,45</sup> The blue dash arrows obviously pointed out that the corresponding adsorption potential of Cu-30 negatively shifted compared with those of CuO NSs and Cu-100. This shift indicates a stronger adsorption energy with the dissociative CO<sub>2</sub> on Cu-30 surface, which facilitated the C-C coupling process due to the immobilization of the dissociative CO<sub>2</sub> intermediate.<sup>44,45,47,48</sup> It is well matched with previous reports that the presence of partially oxidized Cu<sup>+</sup> species on the surface generally lowers the activation energy to adsorb the dissociative CO<sub>2</sub>.<sup>42,49</sup> Therefore, we conclude that the rough Cu surface formed on Cu-30 by the microwave treatment has great impact on the enlargement of surface area and the formation of the partially oxidized Cu species as active sites, promoting the C-C coupling process to enhance the CO<sub>2</sub>RR performances.

## Conclusion

Herein, we developed a facile microwave irradiation method to prepare the oxide-derived Cu NSs. Extra-addition of Cu precursor generated a rough surface with nano-domains deposited on the pristine Cu NSs. The partially oxidized Cu<sup>+</sup> state could be distinctively observed on the XPS spectrum of Cu-30. Due to the large surface area and the presence of Cu<sup>+</sup> species, the FE<sub>C<sub>2+</sub></sub> of Cu-30 could be improved up to 72 % and the partial current density for C<sub>2+</sub> products could reach up to 55 mA cm<sup>-2</sup>. This facile microwave-assisted fabrication method will give a direction to cost-effective design of oxide-derived Cu catalyst for efficient synthesis of C<sub>2+</sub> products by CO<sub>2</sub>RR.

## Acknowledgements

This work was supported by the Research Grants Council (16310419, 16309418, and 16304821), Innovation and Technology Commission (Grant No. ITC-CNERC14EG03) of the Hong Kong Special Administrative Region, and Hong Kong Branch of National Precious Metals Material Engineering Research Centre, City University of Hong Kong.

## Conflict of Interest

The authors declare no conflict of interest.

## Keywords

Copper nanosheet [?] electrochemical CO<sub>2</sub> reduction [?] C<sub>2+</sub> selectivity [?] microwave irradiation

## Reference

1. Shih CF, Zhang T, Li J, Bai C. Powering the future with liquid sunshine. *Joule* . 2018;2(10):1925-1949.
2. Goepfert A, Czaun M, Prakash GS, Olah GA. Air as the renewable carbon source of the future: an overview of CO<sub>2</sub> capture from the atmosphere. *Energy Environ Sci* . 2012;5(7):7833-7853.
3. Dinh C-T, Burdyny T, Kibria MG, et al. CO<sub>2</sub>electroreduction to ethylene via hydroxide-mediated copper catalysis at an abrupt interface. *Science* . 2018;360(6390):783-787.
4. García de Arquer FP, Dinh C-T, Ozden A, et al. CO<sub>2</sub>electrolysis to multicarbon products at activities greater than 1 A cm<sup>-2</sup>. *Science* . 2020;367(6478):661-666.
5. Li F, Li YC, Wang Z, et al. Cooperative CO<sub>2</sub>-to-ethanol conversion via enriched intermediates at molecule-metal catalyst interfaces. *Nat Catal* . 2020;3(1):75-82.
6. Wang X, Wang Z, García de Arquer FP, et al. Efficient electrically powered CO<sub>2</sub>-to-ethanol via suppression of deoxygenation. *Nat Energy* . 2020;5(6):478-486.
7. Nitopi S, Bertheussen E, Scott SB, et al. Progress and perspectives of electrochemical CO<sub>2</sub> reduction on copper in aqueous electrolyte. *Chem Rev* . 2019;119(12):7610-7672.

8. Hori Y, Murata A, Takahashi R. Formation of hydrocarbons in the electrochemical reduction of carbon dioxide at a copper electrode in aqueous solution. *J Chem Soc* . 1989;85(8):2309-2326.
9. Morales-Guio CG, Cave ER, Nitopi SA, et al. Improved CO<sub>2</sub> reduction activity towards C<sub>2+</sub> alcohols on a tandem gold on copper electrocatalyst. *Nat Catal* . 2018;1(10):764-771.
10. Scholten F, Sinev I, Bernal M, Roldan Cuenya B. Plasma-modified dendritic Cu catalyst for CO<sub>2</sub> electroreduction. *ACS Catal* . 2019;9(6):5496-5502.
11. Liu J, Fu J, Zhou Y, Zhu W, Jiang L-P, Lin Y. Controlled synthesis of EDTA-modified porous hollow copper microspheres for high-efficiency conversion of CO<sub>2</sub> to multicarbon products. *Nano Lett* . 2020;20(7):4823-4828.
12. Grosse P, Gao D, Scholten F, Sinev I, Mistry H, Roldan Cuenya B. Dynamic changes in the structure, chemical state and catalytic selectivity of Cu nanocubes during CO<sub>2</sub> electroreduction: size and support effects. *Angew Chem Int Ed* . 2018;57(21):6192-6197.
13. Franco F, Rettenmaier C, Jeon HS, Cuenya BR. Transition metal-based catalysts for the electrochemical CO<sub>2</sub> reduction: from atoms and molecules to nanostructured materials. *Chem Soc Rev* . 2020;49(19):6884-6946.
14. Zou L, Zhong G, Nie Y, et al. Porous Carbon Nanosheets Derived from ZIF-8 Treated with KCl as Highly Efficient Electrocatalysts for the Oxygen Reduction Reaction. *Energy Technol* . 2021;9(4):2100035.
15. Zhao Q, Wang Y, Li M, et al. Organic frameworks confined Cu single atoms and nanoclusters for tandem electrocatalytic CO<sub>2</sub> reduction to methane. *SmartMat* . 2022;3(1):183-193.
16. Li Y, Sun Q. Recent advances in breaking scaling relations for effective electrochemical conversion of CO<sub>2</sub>. *Adv Energy Mater* . 2016;6(17):1600463.
17. Eilert A, Cavalca F, Roberts FS, et al. Subsurface oxygen in oxide-derived copper electrocatalysts for carbon dioxide reduction. *J Phys Chem Lett* . 2017;8(1):285-290.
18. Dutta A, Rahaman M, Luedi NC, Mohos M, Broekmann P. Morphology matters: tuning the product distribution of CO<sub>2</sub> electroreduction on oxide-derived Cu foam catalysts. *ACS Catal* . 2016;6(6):3804-3814.
19. Lyu Z, Zhu S, Xie M, et al. Controlling the surface oxidation of Cu nanowires improves their catalytic selectivity and stability toward C<sub>2+</sub> products in CO<sub>2</sub> reduction. *Angew Chem Int Ed* . 2021;60(4):1909-1915.
20. Gao D, Zegkinoglou I, Divins NJ, et al. Plasma-activated copper nanocube catalysts for efficient carbon dioxide electroreduction to hydrocarbons and alcohols. *ACS nano* . 2017;11(5):4825-4831.
21. Pique O, Vines F, Illas F, Calle-Vallejo F. Elucidating the structure of ethanol-producing active sites at oxide-derived Cu electrocatalysts. *ACS Catal* . 2020;10(18):10488-10494.
22. Dattila F, Garcia-Muelas R, Lopez Nr. Active and selective ensembles in oxide-derived copper catalysts for CO<sub>2</sub> reduction. *ACS Energy Lett* . 2020;5(10):3176-3184.
23. Sun S, Kong C, You H, Song X, Ding B, Yang Z. Facet-selective growth of Cu-Cu<sub>2</sub>O heterogeneous architectures. *CrystEngComm* . 2012;14(1):40-43.
24. Choi C, Kwon S, Cheng T, et al. Highly active and stable stepped Cu surface for enhanced electrochemical CO<sub>2</sub> reduction to C<sub>2</sub>H<sub>4</sub>. *Nat Catal* . 2020;3(10):804-812.
25. Kim T, Palmore GTR. A scalable method for preparing Cu electrocatalysts that convert CO<sub>2</sub> into C<sub>2+</sub> products. *Nat Commun* . 2020;11(1):1-11.
26. Raciti D, Livi KJ, Wang C. Highly dense Cu nanowires for low-overpotential CO<sub>2</sub> reduction. *Nano Lett* . 2015;15(10):6829-6835.

27. Jiang K, Huang Y, Zeng G, Toma FM, Goddard III WA, Bell AT. Effects of surface roughness on the electrochemical reduction of CO<sub>2</sub> over Cu. *ACS Energy Lett* . 2020;5(4):1206-1214.
28. Lei Q, Zhu H, Song K, et al. Investigating the origin of enhanced C<sub>2+</sub> selectivity in oxide-/hydroxide-derived copper electrodes during CO<sub>2</sub> electroreduction. *J Am Chem Soc* . 2020;142(9):4213-4222.
29. Zhang B, Zhang J, Hua M, et al. Highly electrocatalytic ethylene production from CO<sub>2</sub> on nanodeficient Cu nanosheets. *J Am Chem Soc* . 2020;142(31):13606-13613.
30. Li X, Chen W-X, Zhao J, Xing W, Xu Z-D. Microwave polyol synthesis of Pt/CNTs catalysts: effects of pH on particle size and electrocatalytic activity for methanol electrooxidation. *Carbon* . 2005;43(10):2168-2174.
31. Zhu H-t, Zhang C-y, Yin Y-s. Rapid synthesis of copper nanoparticles by sodium hypophosphite reduction in ethylene glycol under microwave irradiation. *J Cryst Growth* . 2004;270(3-4):722-728.
32. Teichert J, Doert T, Ruck M. Mechanisms of the polyol reduction of copper (II) salts depending on the anion type and diol chain length. *Dalton trans* . 2018;47(39):14085-14093.
33. Yin M, Wu C-K, Lou Y, et al. Copper oxide nanocrystals. *J Am Chem Soc* . 2005;127(26):9506-9511.
34. Chusuei CC, Brookshier M, Goodman D. Correlation of relative X-ray photoelectron spectroscopy shake-up intensity with CuO particle size. *Langmuir* . 1999;15(8):2806-2808.
35. Kim J, Choi W, Park JW, Kim C, Kim M, Song H. Branched copper oxide nanoparticles induce highly selective ethylene production by electrochemical carbon dioxide reduction. *J Am Chem Soc* . 2019;141(17):6986-6994.
36. Park PW, Ledford JS. The influence of surface structure on the catalytic activity of alumina supported copper oxide catalysts. Oxidation of carbon monoxide and methane. *Appl Catal B* . 1998;15(3-4):221-231.
37. Andersson K, Ketteler G, Bluhm H, et al. Autocatalytic water dissociation on Cu (110) at near ambient conditions. *J Am Chem Soc* . 2008;130(9):2793-2797.
38. Han J, Chang J, Wei R, et al. Mechanistic investigation on tuning the conductivity type of cuprous oxide (Cu<sub>2</sub>O) thin films via deposition potential. *Int J Hydrog Energy* . 2018;43(30):13764-13777.
39. Gao Y, Yang F, Yu Q, et al. Three-dimensional porous Cu@ Cu<sub>2</sub>O aerogels for direct voltammetric sensing of glucose. *Microchim Acta* . 2019;186(3):1-9.
40. Li F, Thevenon A, Rosas-Hernández A, et al. Molecular tuning of CO<sub>2</sub>-to-ethylene conversion. *Nature* . 2020;577(7791):509-513.
41. Jin Z, Wang L, Zuidema E, et al. Hydrophobic zeolite modification for in situ peroxide formation in methane oxidation to methanol. *Science* . 2020;367(6474):193-197.
42. Velasco-Vélez J-J, Jones T, Gao D, et al. The role of the copper oxidation state in the electrocatalytic reduction of CO<sub>2</sub> into valuable hydrocarbons. *ACS Sustain Chem Eng* . 2018;7(1):1485-1492.
43. Liu X, Sun L, Deng W-Q. Theoretical investigation of CO<sub>2</sub> adsorption and dissociation on low index surfaces of transition metals. *J Phys Chem C* . 2018;122(15):8306-8314.
44. Hori Y, Takahashi I, Koga O, Hoshi N. Selective formation of C<sub>2</sub> compounds from electrochemical reduction of CO<sub>2</sub> at a series of copper single crystal electrodes. *J Phys Chem B* . 2002;106(1):15-17.
45. Calle-Vallejo F, Koper MT. Theoretical considerations on the electroreduction of CO to C<sub>2</sub> species on Cu (100) electrodes. *Angew Chem* . 2013;125(28):7423-7426.
46. Lei F, Liu W, Sun Y, et al. Metallic tin quantum sheets confined in graphene toward high-efficiency carbon dioxide electroreduction. *Nat Commun* . 2016;7(1):1-8.

47. Becerra JG, Salvarezza RC, Arvia AJ. The influence of slow  $\text{Cu}(\text{OH})_2$  phase formation on the electrochemical behaviour of copper in alkaline solutions. *Electrochim Acta* . 1988;33(5):613-621.

48. Strehblow H-H, Maurice V, Marcus P. Initial and later stages of anodic oxide formation on Cu, chemical aspects, structure and electronic properties. *Electrochim Acta* . 2001;46(24-25):3755-3766.

49. Soon A, Todorova M, Delley B, Stampfl C. Oxygen adsorption and stability of surface oxides on Cu (111): A first-principles investigation. *Phys Rev B* . 2006;73(16):165424.

**Figure 1.** TEM images of (a-b) CuO NS, OD-Cu NSs (c) Cu-30, and (d) Cu-100 (the marks of white circles mean the nano-domains.), respectively. (e) XRD patterns of CuO NS, Cu-30, and Cu-100 (the label of star (\*) and hashtag (#) represent metallic Cu and CuO phase, respectively)

**Figure 2 .** XPS spectra at (a) Cu  $2p_{2/3}$  and (b) Cu LMM Auger region of commercial Cu NP, CuO NS, Cu-30, and Cu-100

**Figure 3.** Electrochemical  $\text{CO}_2\text{RR}$  performance of commercial Cu NP, CuO NS, Cu-30, and Cu-100. (a) LSV curves of Cu-30 in the  $\text{CO}_2$ - and Ar- saturated 0.1 M  $\text{KHCO}_3$  electrolyte after 1hr electrolysis. (b) Overall Faradaic efficiencies at a potential of -1.1 V vs. RHE, partial faradaic efficiency (FE) for (c)  $\text{C}_2\text{H}_4$  and (d)  $\text{C}_2+$  products, (e) partial current density of total  $\text{C}_2+$  products.

**Figure 4.** (a) Double layer charge capacitance in  $\text{CO}_2$ -saturated 0.1 M  $\text{KHCO}_3$  electrolyte and (b)  $\text{OH}_{\text{ads}}$  peaks from LSV curves obtained in Ar-saturated 0.1 M KOH electrolyte of commercial Cu NP, pristine CuO NS, Cu-30, and Cu-100. The inset image shows a magnified section of the (111) shoulder peak between 0.42-0.53  $\text{V}_{\text{RHE}}$ .

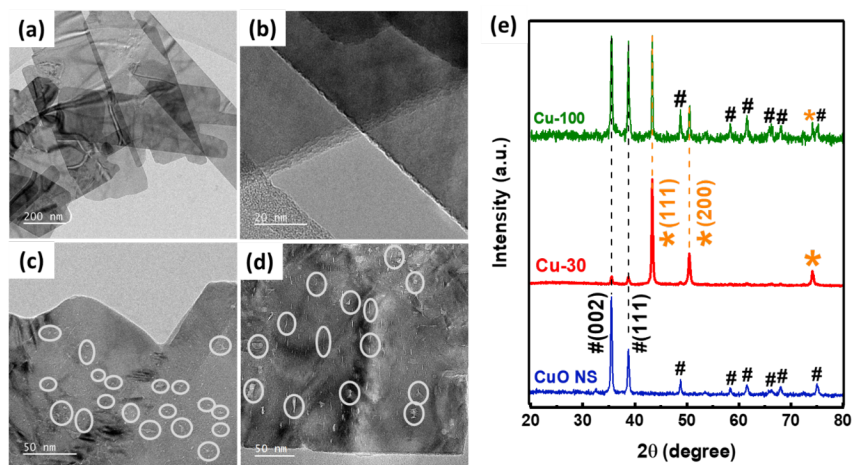


**Figure 1.** TEM images of (a-b) CuO NS, OD-Cu NSs (c) Cu-30, and (d) Cu-100 (the marks of white circles mean the nano-domains.), respectively. (e) XRD patterns of CuO NS, Cu-30, and Cu-100 (the label of star (\*) and hashtag (#) represent metallic Cu and CuO phase, respectively)

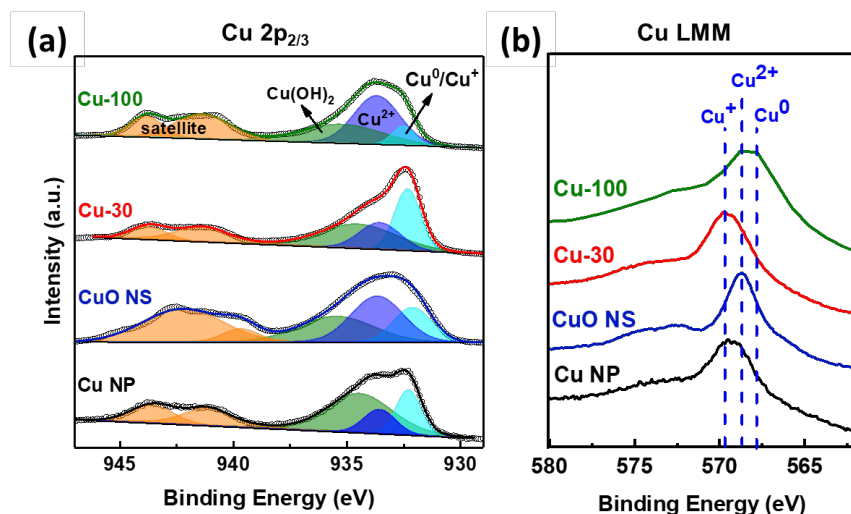


**Figure 2** . XPS spectra at (a) Cu 2p<sub>2/3</sub> and (b) Cu LMM Auger region of commercial Cu NP, CuO NS, Cu-30, and Cu-100

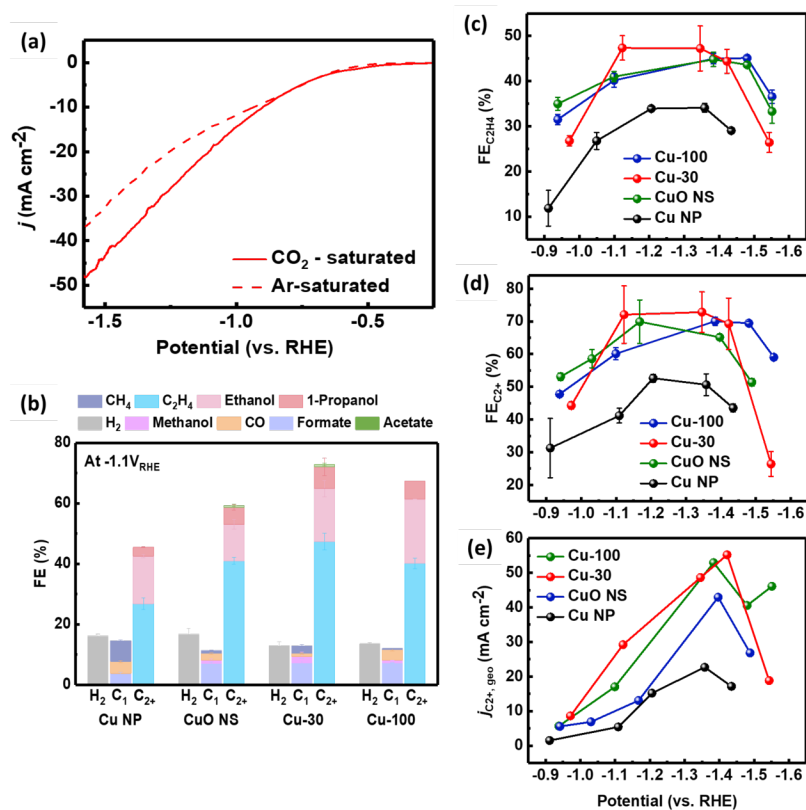


**Figure 3**. Electrochemical CO<sub>2</sub>RR performance of commercial Cu NP, CuO NS, Cu-30, and Cu-100. (a) LSV curves of Cu-30 in the CO<sub>2</sub>- and Ar-saturated 0.1 M KHCO<sub>3</sub> electrolyte after 1 hr electrolysis. (b)

Overall Faradaic efficiencies at a potential of -1.1 V vs. RHE, partial faradaic efficiency (FE) for (c)  $C_2H_4$  and (d)  $C_2+$  products, (e) partial current density of total  $C_2+$  products.

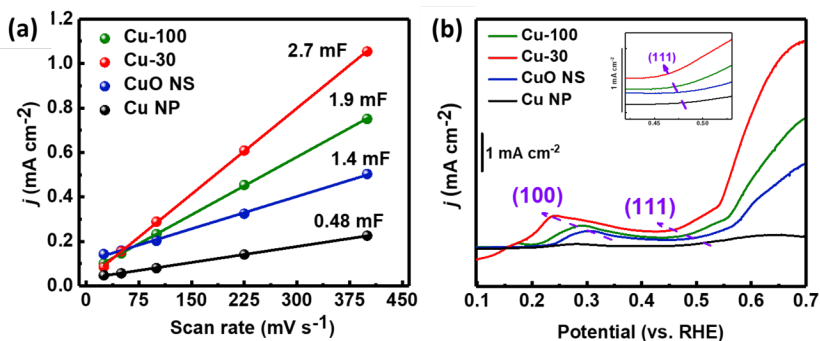


**Figure 4.** (a) Double layer charge capacitance in  $CO_2$ -saturated 0.1 M  $KHCO_3$  electrolyte and (b)  $OH_{ads}$  peaks from LSV curves obtained in Ar-saturated 0.1 M  $KOH$  electrolyte of commercial Cu NP, pristine CuO NS, Cu-30, and Cu-100. The inset image shows a magnified section of the (111) shoulder peak between 0.42-0.53 V<sub>RHE</sub>.

